


Distal-scanning common path probe for optical coherence tomography

Zhengyu Chen ^{*,†}, Bin He^{*,†}, Zichen Yin^{*,†}, Zhangwei Hu^{*,†},
Yejiang Shi^{*,†}, Chengming Wang^{*,‡}, Xiao Zhang[§], Ning Zhang[¶],
Linkai Jing^{||}, Guihuai Wang^{||} and Ping Xue^{*,†,**}

^{*}State Key Laboratory of Low-dimensional Quantum Physics and
Department of Physics, Tsinghua University, Beijing, China

[†]Frontier Science Center for Quantum Information, Beijing, China

[‡]Jinsp Company Limited, Beijing, China

[§]Beijing Institute of Technology, Beijing, China

[¶]Institute of Forensic Science, Ministry of Public Security
Beijing, China

^{||}Department of Neurosurgery, Beijing Tsinghua Changgung Hospital
School of Clinical Medicine and Institute of Precision Medicine
Tsinghua University, Beijing, China

^{**}xuep@tsinghua.edu.cn

Received 13 November 2023

Accepted 26 December 2023

Published 9 February 2024

In this paper, we present a distal-scanning common path probe for optical coherence tomography (OCT) equipped with a hollow ultrasonic motor and a simple and specially designed beam-splitter. This novel probe proves to be able to effectively circumvent polarization and dispersion mismatch caused by fiber motion and is more robust to a variety of interfering factors during the imaging process, experimentally compared to a conventional noncommon path probe. Furthermore, our design counteracts the attenuation of backscattering with depth and the fall-off of the signal, resulting in a more balanced signal range and greater imaging depth. Spectral-domain OCT imaging of phantom and biological tissue is also demonstrated with a sensitivity of ~ 100 dB and a lateral resolution of $\sim 3 \mu\text{m}$. This low-cost probe offers simplified system configuration and excellent robustness, and is therefore particularly suitable for clinical diagnosis as one-off medical apparatus.

Keywords: Common path; optical coherence tomography; endoscopic probe.

1. Introduction

Optical coherence tomography (OCT) is a high-resolution and nondestructive 3D imaging technology widely used in biomedical research and clinical applications.¹⁻⁷ By combining with endoscopic probes, OCT has been extended from ophthalmology,¹ neurosurgery,² and dermatology^{3,4} to *in vivo* imaging of internal organs, such as cardiovascular system,⁵ airways,⁶ and gastrointestinal tract.⁷ During imaging, mechanical vibrations caused by rotation and pullback may result in polarization and dispersion mismatch between the reference arm and sample arm.⁸ Therefore, improving the vibration tolerance of the imaging system to obtain high-quality images is a critical issue in endoscopic OCT.

The common path design has been demonstrated to improve the stability of imaging systems^{9,10} and is more compact, simple, and cost-effective than traditional designs that use polarization-maintaining fibers (PMFs) and polarization controllers. In some clinical applications, disposable probes are used to meet safety and health standards. The common path structure allows for easy replacement of detachable sample probes of any length without worrying about the length mismatch between the reference arm and the sample arm. There is also no need to adjust the reference arm to achieve polarization and dispersion matching after replacing the probe.⁸ In early common path probe designs, the Fresnel reflection at the fiber tip was used as the reference light, while power adjustment was achieved by selection of the polishing angle of the fiber tip to achieve better system sensitivity.^{11,12} To provide higher lateral resolution, various methods can be employed such as chemical etching to fabricate negative axicon,¹³ conical lens,^{14,15} or installing barium titanate microspheres at the fiber tip.¹⁶ Using the light reflected from the surfaces of graded-index (GRIN) lenses,¹⁷ ball-shaped lenses¹⁸ as a reference is also an option. By adding a right-angle prism to reflect the light beam, the aforementioned forward-looking probes can be converted into side-looking probes.¹⁸ However, this approach has a large optical path difference between the reference and the sample arm, causing increased signal frequency, reduced dynamic range, and even artifacts. As a result, the quality of OCT images will be greatly degraded due to the limited spectral resolution in the spectral domain (SD)-OCT and sampling frequency in swept-source (SS)-OCT.¹⁹

This problem can be solved by adding additional circulators and reflectors,¹⁹ or circular-obscuration apodization design,^{20,21} at the expense of increasing system complexity and cost. In addition, common path probes for circumferential scanning are all based on proximal scanning, which can be affected by irregular passageways in clinical applications, resulting in distortion and artifacts in OCT images.

In this study, we demonstrate an endoscopic probe for common path OCT based on a hollow ultrasonic motor.^{22,23} The common path design for a side-looking probe is achieved with simple and low-cost optical components. It successfully avoids the complex processes of chemical etching and optical machining, and also the problem of large optical path differences between the reference and the sample arm. To the best of our knowledge, this is the first common path distal-scanning endoscopic probe. Through comparative experiments, it has been demonstrated that this novel probe can maintain polarization and dispersion matching even during fiber motion. Imaging of biological tissues is also achieved with the probe.

2. Materials and Methods

2.1. Common path probe design

Figure 1(a) illustrates the schematic diagram of the common path probe. The main body of the hollow ultrasonic motor is composed of an aluminum pedestal, a brass square column and a steel stator. Four pieces of piezoelectric plates are bonded to the sides

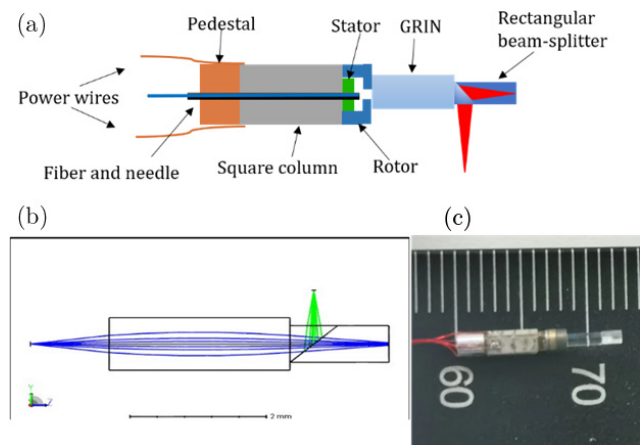


Fig. 1. (a) Schematic of the common path probe. (b) Optical simulation. (c) Photograph of the fabricated common path probe.

of the brass square column with glue. The center of the motor contains a hollow channel with a diameter of $\sim 250 \mu\text{m}$, which allows the optical fiber and protection needle to pass through. A 0.25-pitch GRIN lens and a machined rectangular beam-splitter are fixed on the magnet rotor using UV-cured adhesive. The light emitted from the optical fiber is first focused by the GRIN lens and then split on a coated inclined surface in the beam-splitter. The transmitted light reflects back along the same path at the right end surface of the rectangular beam-splitter and acts as the reference light. Figures 1(b) and 1(c) show the optical simulation and photograph of the fabricated common path probe, respectively. The distance between the GRIN lens and the optical fiber affects the focus position. The greater the distance, the closer the focus position, meaning a shorter working distance. Therefore, in the design process, we initially determined the working distance of the probe and the length of the GRIN lens. Based on these parameters, we established the distance between the lens and the fiber. This also helped in determining the length of the beam splitter, ensuring that the reference light could be coupled back into the fiber as efficiently as possible. The diameter of the probe is 2 mm and the length is about 13 mm. It is worth mentioning that the size of the ultrasonic motor can be further reduced to less than 1 mm in diameter.²² In contrast to the traditional design, where the reference arm has a shorter optical path than the sample arm, our probe has the optical path length of the reference arm greater than that of the sample arm. This change enables the signal from deep tissue to correspond to a lower frequency and therefore have little fall-off. This is equivalent to signal enhancement of the signal from deep tissue, compared to the traditional design where the signal from deep tissue has severe fall-off while backscattering attenuates quickly with depth. So, our design counteracts the attenuation of backscattering with depth and the fall-off of the signal, resulting in a more balanced signal range and greater imaging depth.

2.2. Optical coherence tomography system

An SD-OCT system was built to validate the imaging capability of this common path probe, as shown in Fig. 2(a). The light source is a broadband

super luminescent diode (SLD) (Inphenix, Inc., Livermore, California, USA) with output power of 6.5 mW and bandwidth of 90 nm centered at 850 nm. The light emitted from the SLD was directly coupled to the probe through a circulator. The light returning from the probe passed through the circulator again and reached the spectrometer, where we employed a wavenumber-linear spectrometer to avoid the need for wavenumber linearization in post-processing. The signal light was finally detected by a 2048-pixel line scan CMOS camera (Teledyne-e2v, OCTPLUS, UK) with a line rate of 117 kHz and an integration time of $8.3 \mu\text{s}$. Meanwhile, we also built a traditional SD-OCT system equipped with a noncommon path probe, as shown in Fig. 2(b). Differing from the system illustrated in Fig. 2(a), the light emitted from port 2 of the circulator would pass through an optical fiber coupler. One output of the coupler directed the light to the noncommon path probe. The light emitted from another output passed through a collimator and a lens, then was reflected by a mirror.

2.3. Stability analysis experiment

For noncommon path probe, the polarization controllers need to be adjusted to match the polarization of the two arms to maximize the signal peak. However, as previously mentioned, the rotation and pullback of the sample arm may inevitably cause vibrations, changing the polarization state of the sample arm fiber. To evaluate the impact of fiber vibrations on imaging quality and demonstrate that our new design can overcome polarization mismatches caused by motion, we conducted a comparative experiment by imaging a mirror under the common path and noncommon path conditions. The corresponding systems are shown in Figs. 2(a) and 2(b). Continuous measurement of the point spread function (PSF) of a mirror was performed while quickly shaking fibers. The experimental results are shown in Fig. 3.

2.4. Imaging experiments

We conducted imaging experiments on phantoms and biological tissues to evaluate the imaging capability of the common path probe. First, we imaged a phantom, which was made by coiling translucent tape (Scotch, 3M, Saint Paul, Minnesota, US) on a glass tube. The A-line rate and integration time

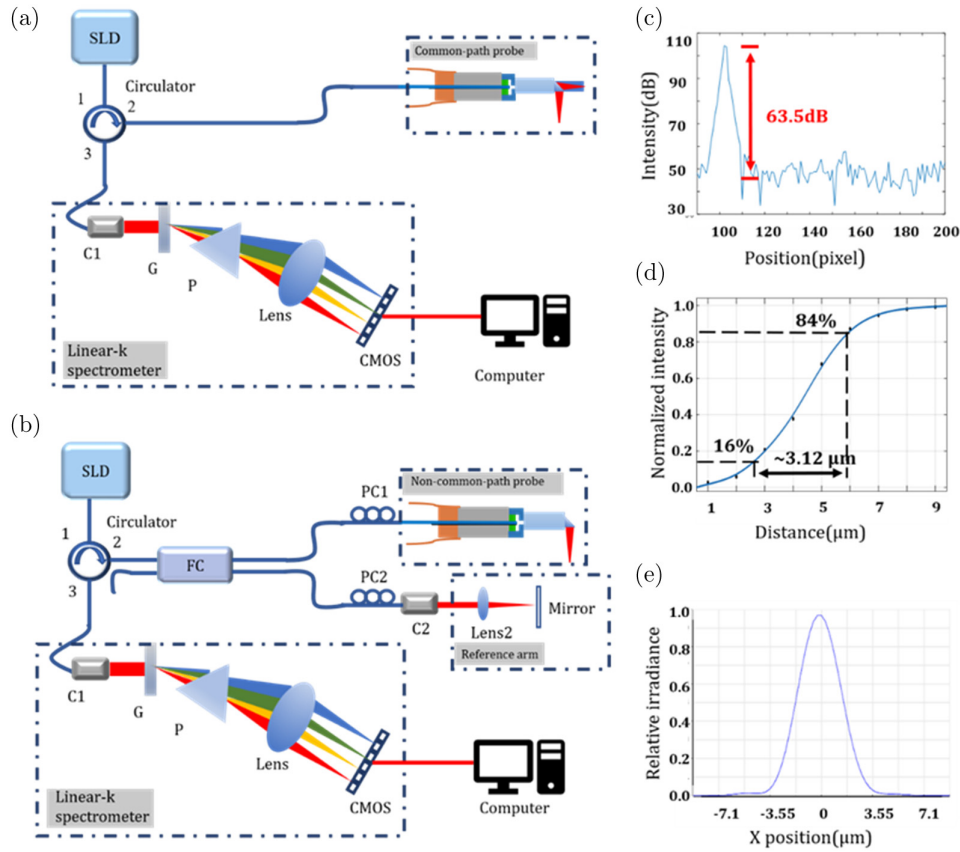


Fig. 2. (a) Schematic of the common path endoscopic SD-OCT system. (b) Schematic of traditional endoscopic SD-OCT system. (c) The return signal of 63.5 dB from the mirror after an attenuation of 36.4 dB. (d) The light transmission intensity against the moving distance of a sharp edge. Measurement of the lateral resolution defined as the 16–84% bandwidth of the curve. (e) Huygens PSF. C, collimator; G, grating; FC, fiber coupler; P, triple prism; PC, polarization controller.

of the camera were set to be 117 kHz and 8.3 μs . The rotation speed of the probe was 36.56 r/s, so each image consisted of ~ 3200 A-lines. Next, we dug a hole in an onion with an annular blade of 1.5 mm

diameter and inserted the probe to acquire images, using the same integration time and image data processing as for the phantom imaging. The experimental results are shown in Fig. 4.

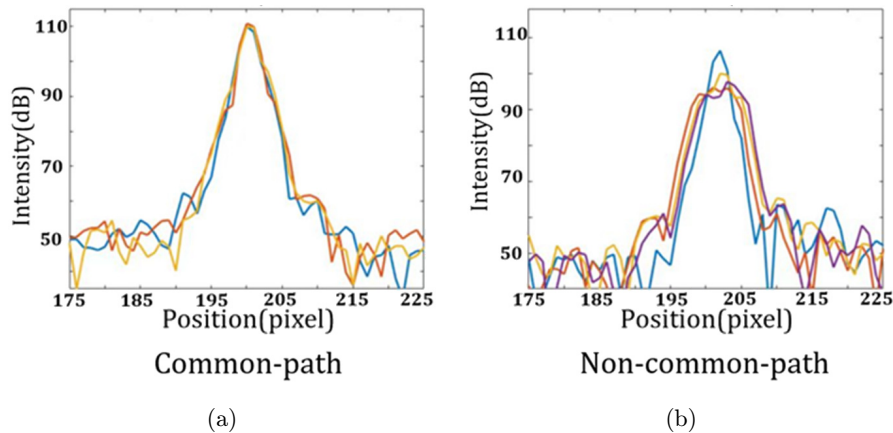


Fig. 3. PSF stability analysis with polarization and dispersion change. (a) Imaging results under the common path condition. (b) Imaging results under the noncommon path condition. Each color represents one different measurement.

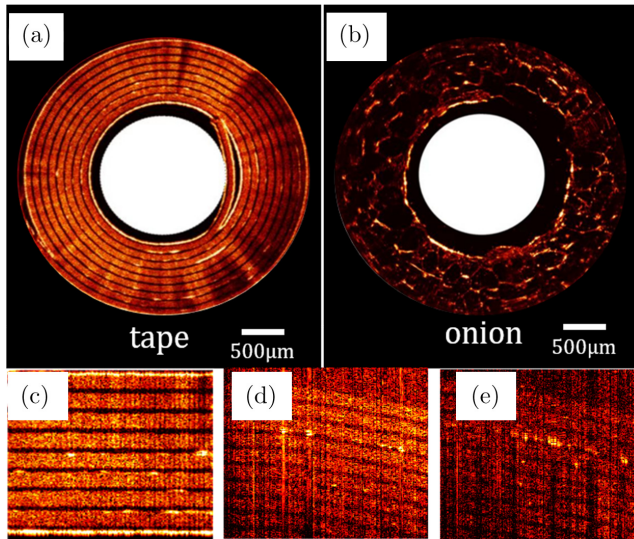


Fig. 4. OCT images obtained with probes. (a)–(c) are images obtained with the common path probe. (d) and (e) are images obtained with the noncommon path probe. (a) The phantom of translucent tape. (b) OCT image of an onion. (c) Part of (a). (d) The phantom of translucent with polarization matching. (e) The phantom of translucent with polarization mismatching.

3. Results

3.1. Common path probe driven by a hollow ultrasonic motor

Ultrasonic motors utilize the inverse piezoelectric effect of piezoelectric plates.^{22,24} When a positive or negative voltage is applied to a piezoelectric plate, the plate correspondingly elongates or contracts. Therefore, when a sinusoidally varying voltage is applied, the plate undergoes periodic elongation and contraction. By applying sinusoidal voltages of the same frequency to the four piezoelectric plates on the stator, but with a phase difference of $\pi/2$ between adjacent plates, they each undergo their periodic motion, but elongate to their maximum values sequentially in time. The rotor of the ultrasonic motor, designed to match the stator's edge, is made of magnetic material. Hence, a magnetic force exists between it and the stator's steel ring, providing a preload. When the stator vibrates at a fixed period, there is always a contact point between the rotor and stator at any given moment. This point is where the plate causes the stator to elongate to its maximum value. The frictional force generated by the aforementioned preload at this point can accelerate the rotor tangentially. This action drives the rotor, resulting in stable rotation, much like how a person uses waist movements to rotate a

hula hoop. Compared with traditional motorized distal-scanning probes, the ultrasonic motor can be designed to be hollow, allowing fiber to pass through. So, the motor's position can be moved to the front of the GRIN lens, and the wires of the motor will not pass through the imaging field of view. Therefore, 360° unobstructed circular imaging can be achieved. In OCT imaging, the power and optical path length of the reference light can affect the sensitivity of the imaging. In this design, the coating types, the size of the rectangular beam-splitter, and the shape of its top surface can be easily determined to achieve optimal sensitivity if light source and camera model are predetermined.

3.2. Simplified system structure and operational requirements

As shown in Fig. 2, OCT system equipped with common path probe can save one fiber coupler, two polarization controllers and the optics for an additional spatial optical path of the reference arm. This design not only reduces the system cost but also simplifies its structure and hence enhances its stability. Then we tested the system performance. After an attenuation of 36.4 dB, the measured signal-to-noise ratio (SNR) is 63.5 dB, as shown in Fig. 2(c), so the system sensitivity is ~ 100 dB. To measure the lateral resolution of the probe, a sharp-edge blade was used and moved across at the focal position. The light transmission against the moving distance of the blade is shown in Fig. 2(d). The 16–84% width of the slope region, which is equal to the beam waist radius at which the intensity attenuates to $1/e^2$ of the central intensity, is also defined as the lateral resolution. The measured result is $3.12 \mu\text{m}$, slightly larger than the simulated result of $2.95 \mu\text{m}$, as shown in Fig. 2(e). Moreover, unlike the conventional noncommon path probe which often suffers from large dispersion mismatch between reference and sample arm, our probe is able to optimize dispersion matching and thus there is no need for hardware and software dispersion compensation as is needed in the conventional system. As we know, the probes should generally be single-use device in clinical applications. Each time to use a new probe, it is necessary to re-adjust the reference arm, software parameters and dispersion compensation again. However, with our common path design, each new probe is automatically optimized for

dispersion compensation and no re-adjustment is needed to achieve high-quality image. This really means that our probe is a plug-and-play probe. Therefore, our novel probe can not only reduce the difficulty of clinical examinations but also save the computational cost of dispersion compensation, and is therefore particularly suitable for clinical diagnosis as one-off medical apparatus.

3.3. *Stable polarization matching under fiber motion*

Polarization matching is crucial for achieving high-quality imaging; therefore, before imaging with a traditional probe, it is necessary to adjust the polarization controllers on both arms. While adjusting the polarization controllers can match the polarization of the two arms under static conditions, it is hardly possible to compensate the dynamic changes in polarization due to movement during high-speed imaging, resulting in a decrease in signal intensity and image quality as well. The results of a comparative experiment by imaging a mirror illustrated this problem. We used different colors to represent the mirror image at different times. For a noncommon path probe, as shown in Fig. 3(b), the blue line with the highest intensity represented the signal before shaking the fiber, because the polarization states of the two arms were equal after adjusting the polarization controllers and thus the signal was optimal. However, when shaking fibers, there was nearly a 10 dB decrease of the signal amplitude. At the same time, the signal width, i.e., the axial resolution, also deteriorated to some extent due to the changes of dispersion and polarization caused by the irregular bending of fibers. It is obvious that the static dispersion compensation cannot compensate for the dynamic dispersion changes due to the uncontrollable movement of fibers, leading to signal broadening. In contrast, our probe was quite robust to the movement of fibers and therefore the signal peak and width remained stable throughout all the measuring process, as shown in Fig. 3(a). Therefore, we have verified that this probe has a high tolerance to vibrations and can avoid image quality deterioration caused by polarization and dispersion mismatch, making it more suitable for three-dimensional imaging of complex tubular structures within the body.

3.4. *Imaging results on phantoms and biological tissues*

As shown in Fig. 4(a), the multilayered structure of the tape was clearly visible. Furthermore, the use of the hollow ultrasonic motor allowed for unobstructed 360° imaging, which could ensure complete imaging of lesion areas without the obstruction of wires. The relatively dark areas in the deeper parts of the tape were caused by strong reflections from one of its surfaces. As shown in Fig. 4(b), the cellular walls of the onion were also clearly visible throughout the entire imaging field. It was worth mentioning that the image was quite steady during the imaging scan, owing to the interference robustness of the common path probe. The partial loss and blurring of the structure in the shallow area were due to damage caused by the blade during the cutting process. Figures 4(d) and 4(e) show the imaging results of the noncommon path probe on tape. As previously mentioned, for the noncommon path probe, there is significant dispersion between the sample and reference arms, therefore it is necessary to use software methods to remove the background and perform dispersion compensation. When the light returning from the surface of the probe's optical components is not eliminated by the angled cuts of the fiber and the GRIN lens and fluctuates in intensity during rotation, software compensation may not be effective, adversely impacting the image quality. The noise in Figs. 4(d) and 4(e) is an example of this issue. In contrast, common path probe does not require software-based dispersion compensation. Furthermore, Figs. 4(d) and 4(e) represent imaging results under polarization-matched and polarization-mismatched conditions, respectively. The significant intensity difference between the two clearly illustrates the importance of maintaining polarization matching during the imaging process. Another advantage of our design is that the OCT signal is more uniformly distributed throughout all the depth because our design counteracts the attenuation of backscattering with depth and the fall-off of the signal. Our imaging system has a 6 dB fall-off at 1.27 mm.²⁵ Unlike typical OCT system, if we set the optical path length of the reference arm longer than that of the sample surface by 1.27 mm, the signal reflected from the depth of 1.27 mm will not suffer from fall-off effect, equivalent to a SNR enhancement of ~ 6 dB. As we can see, both Figs. 4(a) and 4(b) had

more uniform brightness from the surface to the deep and are more likely to real biopsy, compared to conventional SD-OCT image like Fig. 3(a) in Ref. 23. In fact, the equivalent SNR enhancement for deep depth also results in a larger imaging depth, because more signal of deep depth can be detected due to the enhancement. It is obvious that the imaging results have successfully demonstrated the excellent capability of the common path probe for imaging biological tissues.

4. Discussion

In traditional common path probe design, the light reflected from the fiber tip or the surfaces of GRIN lens are used as the reference. To improve SNR and lateral resolution, complex etching and processing of the probe tip are required. Such a scheme is commonly used in forward-looking probe applications. This design concept can also be applied to side-looking probes by adding right-angle prism for light deflection. However, a significant challenge arises due to the large optical path difference between the two arms, resulting in reduced image dynamic range. Moreover, circumferential-scanning common path probes are typically based on proximal scanning, which is more prone to image distortion compared to distal scanning. The new design we propose in this paper can address these issues mentioned above.

First, the fabrication and installation of a rectangular beam-splitter are straightforward and do not impose any additional requirements on the overall probe structure. By replacing the right-angle prism with a beam-splitter, the traditional probe can be converted into a common path probe.

Second, by adjusting the dimensions and coatings of the beam splitter, we can regulate the optical power and path length of the reference light to meet the requirements for high-quality imaging. In this validation experiment, we chose a commercially available rectangular beam-splitter to avoid additional processing. The proportion of transmitted light and reflected light on the interface was 50:50, therefore we had to adjust the distance between the fiber tip and the GRIN lens to reduce the reference light back into the fiber to avoid extra noise and achieve high sensitivity. This results in a loss of optical power, which is equivalent to a ~ 5 dB attenuation in SNR. In the future, we will modify the coating of the beam-splitter to reduce the

reference light and increase the sample light and hence further improve the system sensitivity. After optimization, the system sensitivity can reach more than 105 dB. In addition, the new design eliminates the large optical path difference between the two arms without additional circulators and reflectors, or circular-obscuration apodization design, reducing the effect of fall-off.

Third, we have first achieved the distal scanning common path probe. In proximal scanning, optical fibers are often affected by bending and pressure changes during high-speed rotation, leading to changes in refractive index and adverse effects on imaging, such as distortion. Therefore, compared to previous common path probes, imaging stability with our new probe is further improved.

Meanwhile, our probe has the optical path length of the reference arm greater than that of the sample arm to enhance the signal from deep tissue. In our experiment, the initial design featured the reference arm's optical path being about 1 mm longer than that of the sample arm. However, to reduce the power of the reference arm, I shortened the distance between the lens and the fiber in the experiment. This adjustment was measured as a 0.23 mm change on the translation stage scale. Therefore, the optical path length of the reference arm is correspondingly reduced. The current imaging depth was limited because the optical path length of the reference arm was only ~ 0.8 mm longer than that of the sample surface by using this commercial beam-splitter, which is less than 6 dB fall-off depth of 1.27 mm. We may extend the length of the beam-splitter or alter the materials to increase the optical path length of the reference arm, achieving the enhancement of the signal of deep tissue and thus greater imaging depth. After enlarging the length of the beam-splitter, the focus point along the reference arm may be in front of the right end surface of the beam-splitter. This may lower down the coupling efficiency of the reference light back into the fiber. However, a high coupling efficiency is still possible by polishing the right end surface of the beam-splitter into an optimized spherical surface.

5. Conclusions

In summary, we propose a common path endoscopic probe design for distal-scanning mode based on a hollow ultrasonic motor, which is cost-effective, easy to manufacture and assemble, and allows for

easy optimization of optical power and path length of reference arm for best system sensitivity. The experimental results have demonstrated that the probe can instinctively maintain polarization and dispersion matching during fiber motion and is more robust to a variety of interfere factors during imaging process. Furthermore, this probe counteracts the attenuation of backscattering with depth and the fall-off of the signal, resulting in a more balanced signal range and greater imaging depth. The common path structure allows for easy replacement of detachable sample probes of any length with instinctive match of path length and polarization or dispersion between the reference and the sample arm. There is thus no need to adjust the reference arm after replacing the probe. We believe that this low-cost probe offers simplified system configuration and excellent robustness, and is therefore particularly suitable for clinical diagnosis as one-off medical apparatus.


Acknowledgments

This work was supported in part by the National Natural Science Foundation of China under Grants 61975091, 61905015, 61575108, and 61505034, in part by the Tsinghua Precision Medicine Foundation and “Bio-Brain+X” Advanced Imaging Instrument Development Seed Grant.

Conflicts of Interest

The authors declare that there are no conflicts of interest relevant to this paper.

ORCID

Zhengyu Chen  <https://orcid.org/0009-0005-4103-5765>

References

1. N. Minakaran, E. R. de Carvalho, A. Petzold, S. H. Wong, “Optical coherence tomography (OCT) in neuro-ophthalmology,” *Eye* **35**, 17–32 (2021).
2. B. He, Y. Zhang, Z. Meng, Z. He, Z. Chen, Z. Yin, Z. Hu, Y. Shi, C. Wang, X. Zhang, N. Zhang, G. Wang, P. Xue, “Whole brain micro-vascular imaging using robot assisted optical coherence tomography angiography,” *IEEE J. Sel. Top. Quantum Electron.* **29**, 1–9 (2023).
3. S. Ai, C. Wang, W. Zhang, J.-C. Hsieh, Z. Chen, B. He, X. Zhang, N. Zhang, Y. Gu, P. Xue, “Fully automatic prediction for efficacy of photodynamic therapy in clinical port-wine stains treatment: A pilot study,” *IEEE Access* **8**, 31227–31233 (2020).
4. B. He, Y. Zhang, Z. Meng, Z. He, C. Wang, Z. Chen, Z. Yin, Z. Hu, Y. Shi, N. Zhang, W. Zhang, G. Wang, P. Xue, “Optical coherence tomography angiography with adaptive multi-time interval,” *J. Biophotonics* **16**, e202200340 (2023).
5. Y. Li, S. Moon, Y. Jiang, S. Qiu, Z. Chen, “Intravascular polarization-sensitive optical coherence tomography based on polarization mode delay,” *Sci. Rep.* **12**, 6831 (2022).
6. J. S. Kimbell, S. Basu, G. J. M. Garcia, D. O. Frank-Ito, F. Lazarow, E. Su, D. Protsenko, Z. Chen, J. S. Rhee, B. J. Wong, “Upper airway reconstruction using long-range optical coherence tomography: Effects of airway curvature on airflow resistance: NECK CURVATURE EFFECTS IN LR-OCT IMAGING,” *Lasers Surg. Med.* **51**, 150–160 (2019).
7. T. H. Nguyen, O. O. Ahsen, K. Liang, J. Zhang, H. Mashimo, J. G. Fujimoto, “Correction of circumferential and longitudinal motion distortion in high-speed catheter/endoscope-based optical coherence tomography,” *Biomed. Opt. Express* **12**, 226 (2021).
8. A. B. Vakhtin, D. J. Kane, W. R. Wood, K. A. Peterson, “Common-path interferometer for frequency-domain optical coherence tomography,” *Appl. Opt.* **42**, 6953 (2003).
9. D. Wang, C. Duan, X. Zhang, Z. Yun, A. Pozzi, H. Xie, “Common-path optical coherence tomography using a microelectromechanical-system-based endoscopic probe,” *Appl. Opt.* **55**, 6930 (2016).
10. G. Lan, M. Singh, K. V. Larin, M. D. Twa, “Common-path phase-sensitive optical coherence tomography provides enhanced phase stability and detection sensitivity for dynamic elastography,” *Biomed. Opt. Express* **8**, 5253 (2017).
11. X. Liu, J. U. Kang, “Optimization of an angled fiber probe for common-path optical coherence tomography,” *Opt. Lett.* **38**, 2660 (2013).
12. K. Zhang, W. Wang, J. Han, J. U. Kang, “A surface topology and motion compensation system for micro-surgery guidance and intervention based on common-path optical coherence tomography,” *IEEE Trans. Biomed. Eng.* **56**, 2318–2321 (2009).
13. K. Vairagi, A. Pandey, P. Gupta, R. A. Minz, U. K. Tiwari, J. Fick, S. K. Mondal, “Common-path optical coherence tomography using the Bessel beam from negative Axicon optical fiber tip,” *IEEE J. Sel. Top. Quantum Electron.* **25**, 1–6 (2019).
14. M. Marrese, H. Offerhaus, E. Paardekam, D. Iannuzzi, “70 μm diameter optical probe for

- common-path optical coherence tomography in air and liquids,” *Opt. Lett.* **43**, 5929 (2018).
15. K. M. Tan, M. Mazilu, T. H. Chow, W. M. Lee, K. Taguchi, B. K. Ng, W. Sibbett, C. S. Herrington, C. T. A. Brown, K. Dholakia, “In-fiber common-path optical coherence tomography using a conical-tip fiber,” *Opt. Express* **17**, 2375 (2009).
 16. J.-H. Kim, J.-H. Han, J. Jeong, “Common-path optical coherence tomography using a conical-frustum-tip fiber probe,” *IEEE J. Sel. Top. Quantum Electron.* **20**, 8–14 (2014).
 17. U. Sharma, N. M. Fried, J. U. Kang, “All-fiber common-path optical coherence tomography: Sensitivity optimization and system analysis,” *IEEE J. Sel. Top. Quantum Electron.* **11**, 799–805 (2005).
 18. K. Singh, D. Yamada, G. Tearney, “Common path side viewing monolithic ball lens probe for optical coherence tomography,” *Sovrem Tehnol. Med.* **7**, 29–33 (2015).
 19. J. S. Park, Z. Chen, M. Y. Jeong, C.-S. Kim, “Double common-path interferometer for flexible optical probe of optical coherence tomography,” *Opt. Express* **20**, 1102 (2012).
 20. D. Cui, K. K. Chu, B. Yin, T. N. Ford, C. Hyun, H. M. Leung, J. A. Gardecki, G. M. Solomon, S. E. Birket, L. Liu, S. M. Rowe, G. J. Tearney, “Flexible, high-resolution micro-optical coherence tomography endobronchial probe toward in vivo imaging of cilia,” *Opt. Lett.* **42**, 867 (2017).
 21. K. K. Chu, C. Unglert, T. N. Ford, D. Cui, R. W. Carruth, K. Singh, L. Liu, S. E. Birket, G. M. Solomon, S. M. Rowe, G. J. Tearney, “In vivo imaging of airway cilia and mucus clearance with micro-optical coherence tomography,” *Biomed. Opt. Express* **7**, 2494 (2016).
 22. T. Chen, N. Zhang, T. Huo, C. Wang, J. Zheng, T. Zhou, P. Xue, “Tiny endoscopic optical coherence tomography probe driven by a miniaturized hollow ultrasonic motor,” *J. Biomed. Opt.* **18**, 1 (2013).
 23. W. Liao, T. Chen, C. Wang, W. Zhang, Z. Peng, X. Zhang, S. Ai, D. Fu, T. Zhou, P. Xue, “Endoscopic optical coherence tomography with a focus-adjustable probe,” *Opt. Lett.* **42**, 4040 (2017).
 24. Z. Tieying, “A cylindrical rod ultrasonic motor with 1 mm diameter and its application in endoscopic OCT,” *Chin. Sci. Bull.* **50**(8), 826–830 (2005).
 25. B. He, Y. Zhang, L. Zhao, Z. Sun, X. Hu, Y. Kang, L. Wang, Z. Li, W. Huang, Z. Li, G. Xing, F. Hua, C. Wang, P. Xue, N. Zhang, “Robotic-OCT guided inspection and microsurgery of monolithic storage devices,” *Nat. Commun.* **14**, 5701 (2023).